Monthly Notices
of the
ROYAL ASTRONOMICAL SOCIETY

MNRAS **475,** 1765–1776 (2018)
Advance Access publication 2017 December 13

doi:10.1093/mnras/stx3207

K2-139 b: a low-mass warm Jupiter on a 29-d orbit transiting an active K0 V star

O. Barragán,[1★] D. Gandolfi,[1] A. M. S. Smith,[2] H. J. Deeg,[3,4] M. C. V. Fridlund,[5,6] C. M. Persson,[5] P. Donati,[7] M. Endl,[8] Sz. Csizmadia,[2] S. Grziwa,[9] D. Nespral,[3,4] A. P. Hatzes,[10] W. D. Cochran,[8] L. Fossati,[11] S. S. Brems,[12] J. Cabrera,[2] F. Cusano,[7] Ph. Eigmüller,[1] C. Eiroa,[13] A. Erikson,[2] E. Guenther,[10] J. Korth,[9] D. Lorenzo-Oliveira,[14] L. Mancini,[15,16,17] M. Pätzold,[9] J. Prieto-Arranz,[3,4] H. Rauer,[2,18] I. Rebollido,[13] J. Saario[19] and O. V. Zakhozhay[15,20]

[1]*Dipartimento di Fisica, Universitá di Torino, Via P. Giuria 1, I-10125 Torino, Italy*
[2]*Institute of Planetary Research, German Aerospace Center, Rutherfordstrasse 2, D-12489 Berlin, Germany*
[3]*Instituto de Astrofísica de Canarias, E-38205 La Laguna, Tenerife, Spain*
[4]*Departamento de Astrofísica, Universidad de La Laguna, E-38206 La Laguna, Tenerife, Spain*
[5]*Department of Earth and Space Sciences, Chalmers University of Technology, Onsala Space Observatory, SE-439 92 Onsala, Sweden*
[6]*Leiden Observatory, University of Leiden, PO Box 9513, NL-2300 RA Leiden, the Netherlands*
[7]*INAF – Osservatorio Astronomico di Bologna, Via Ranzani, 1, I-20127 Bologna, Italy*
[8]*Department of Astronomy and McDonald Observatory, University of Texas at Austin, 2515 Speedway, Stop C1400, Austin, TX 78712, USA*
[9]*Rheinisches Institut für Umweltforschung an der Universität zu Köln, Aachener Strasse 209, D-50931 Köln, Germany*
[10]*Thüringer Landessternwarte Tautenburg, Sternwarte 5, D-07778 Tautenburg, Germany*
[11]*Space Research Institute, Austrian Academy of Sciences, Schmiedlstrasse 6, A-8041 Graz, Austria*
[12]*Landessternwarte, Zentrum für Astronomie der Universität Heidelberg, Königstuhl 12, D-69117 Heidelberg, Germany*
[13]*Departamento Física Teórica, Unversidad Autónoma de Madrid, Cantoblanco, E-28049 Madrid, Spain*
[14]*Departamento de Astronomia do IAG/USP, Universidade de São Paulo, Rua do Matão 1226, Cidade Universitária, 05508-900 São Paulo, SP, Brazil*
[15]*Max-Planck-Institut für Astronomie, Königstuhl 17, D-69117 Heidelberg, Germany*
[16]*Department of Physics, University of Rome Tor Vergata, I-00173 Rome, Italy*
[17]*INAF – Astrophysical Observatory of Turin, 10025-Turin, Italy*
[18]*Center for Astronomy and Astrophysics, TU Berlin, Hardenbergstr. 36, D-10623 Berlin, Germany*
[19]*Nordic Optical Telescope, Apartado 474, E-38700 Santa Cruz de La Palma, Spain*
[20]*Main Astronomical Observatory, National Academy of Sciences of the Ukraine, 27 Akademika Zabolotnoho St. 03143, Kyiv, Ukraine*

Accepted 2017 December 5. Received 2017 December 4; in original form 2017 February 2

ABSTRACT

We announce the discovery of K2-139 b (EPIC 218916923 b), a transiting warm-Jupiter ($T_{\rm eq}$ = 547 ± 25 K) on a 29-d orbit around an active ($\log R'_{\rm HK} = -4.46 \pm 0.06$) K0 V star in *K2* Campaign 7. We derive the system's parameters by combining the *K2* photometry with ground-based follow-up observations. With a mass of $0.387^{+0.083}_{-0.075}$ $M_{\rm J}$ and radius of $0.808^{+0.034}_{-0.033}$ $R_{\rm J}$, K2-139 b is one of the transiting warm Jupiters with the lowest mass known to date. The planetary mean density of $0.91^{+0.24}_{-0.20}$ g cm^{-3}can be explained with a core of ∼50 $M_\oplus$. Given the brightness of the host star (V = 11.653 mag), the relatively short transit duration (∼5 h), and the expected amplitude of the Rossiter–McLaughlin effect (∼25m s^{-1}), K2-139 is an ideal target to measure the spin-orbit angle of a planetary system hosting a warm Jupiter.

Key words: planets and satellites: detection – planets and satellites: individual: K2-139 b (EPIC 218916923b) – stars: fundamental parameters – planetary systems.

1 INTRODUCTION

Gas-giant planets ($M_{\rm p} \gtrsim 0.3\,M_{\rm Jup}$, Hatzes & Rauer 2015) with orbital periods ranging between ∼10 and 100 d are called warm Jupiters. They mark the transition between hot Jupiters (giant planets with orbital period between ∼1 and 10 d) and Jupiter analogues (orbital period longer than 100 d). They seem to be less common than hot Jupiters and their formation scenario is still under debate (e.g. Boley, Granados Contreras & Gladman 2016; Frewen & Hansen 2016). Whereas it is commonly accepted that hot Jupiters did not form *in situ* (e.g. Kley & Nelson 2012), but rather formed beyond the

★ E-mail: oscar.barraganvil@edu.unito.it

snow line and then migrated inwards to their current position, it has been recently proposed that warm Jupiters might have formed *in situ* (e.g. Boley, Granados Contreras & Gladman 2016; Huang, Wu & Triaud 2016).

Eighty warm Jupiters have been discovered so far from both ground- (e.g. da Silva et al. 2007; Brahm et al. 2016; Jenkins et al. 2017) and space-based surveys (e.g. Deeg et al. 2010; Saad-Olivera et al. 2017; Smith et al. 2017). About 30 are known to transit their parent star and only 13 have masses and radii known with a precision better than 25 per cent.[1] They have been detected both in low-eccentricity orbits ($e \lesssim 0.4$, e.g. Brahm et al. 2016; Niedzielski et al. 2016; Smith et al. 2017) and in high-eccentric orbits (e.g. Dawson et al. 2012; Ortiz et al. 2015). Dong, Katz & Socrates (2014) found that warm Jupiters with high eccentricities ($e \gtrsim 0.4$) tend to have a massive planetary/stellar companion in a long-period orbit. The architectures of these systems suggest that eccentric warm Jupiters might have reached their current positions via high-eccentricity migration excited by the outer companion (Dong et al. 2014). On the other hand, warm Jupiters with no detected Jovian companion tend to have lower eccentricities peaked around 0.2. This suggests that two different types of warm Jupiters might exist: those formed via high-eccentricity migration and those formed *in situ*. Alternatively, warm Jupiters in low-eccentricity orbits can also result from disc-driven migration from the outer region of the system (Kley & Nelson 2012).

Petrovich & Tremaine (2016) studied the possibility that warm Jupiters are undergoing secular eccentricity oscillations induced by an outer companion in an eccentric and/or mutually inclined orbit. Their model suggests that high-eccentricity migration can account for most of the hot Jupiters, as well as for most of the warm Jupiters with $e \gtrsim 0.4$. However, it cannot account for the remaining population of low-eccentricity warm Jupiters, which must have undergone a different formation mechanism. The low efficiency to generate warm Jupiters in nearly circular orbits via high-eccentricity migration has been corroborated by Hamers et al. (2016) and Antonini, Hamers & Lithwick (2016) using numerical simulations.

In order to test different planet formation mechanisms, we need to characterize the population of warm Jupiters in terms of planetary mass, radius and orbital parameters. We herein present the discovery of K2-139 b (EPIC 218916923 b), a transiting warm Jupiter ($M_{\rm p} = 0.387^{+0.083}_{-0.075}\ M_{\rm J}$, $R_{\rm p} = 0.808^{+0.034}_{-0.033}\ R_{\rm J}$) in a 29-d orbit around an active K0 V star that has been photometrically monitored by the *K2* space-mission during its Campaign 7. We combine the *K2* photometry with ground-based imaging and high-precision radial velocity (RV) measurements to confirm the planet and derive the main parameters of the system.

2 *K2* PHOTOMETRY

K2 Campaign 7 was performed between 2015 October 04 UT and 2015 December 26 UT.[2] The *Kepler* spacecraft was pointed at coordinates $\alpha = 19^{\rm h}11^{\rm m}19^{\rm s}$, $\delta = -23^{\circ}21'36''$. *K2* observed simultaneously 13 469 sources in long-cadence mode (∼30 min integration time) and 72 objects in short-cadence mode (∼1 min integration time), leading to a total of 13 541 light curves.

For the detection of transiting planet candidates, we used the *K2* Campaign 7 light curves[3] extracted by Vanderburg & Johnson (2014). We analysed the light curves using the DST algorithm (Cabrera et al. 2012) and the EXOTRANS pipeline (Grziwa, Pätzold & Carone 2012; Grziwa & Pätzold 2016). Both codes have been used extensively on *CoRoT* (Cabrera et al. 2009; Carpano et al. 2009; Carone et al. 2012; Cavarroc et al. 2012; Erikson et al. 2012) and *Kepler* (Cabrera et al. 2014; Grziwa & Pätzold 2016) data. These search algorithms detect periodic patterns in time series photometric data. DST uses an optimized transit shape with the same number of free parameters as for the BLS algorithm (Box-fitting Least Squares; Kovács, Zucker & Mazeh 2002), and it also implements better statistics for signal detection. EXOTRANS uses the BLS algorithm combined with the wavelet-based filter technique VARLET (Grziwa & Pätzold 2016), diminishing the effects of stellar variability and data discontinuities.

We detected a periodic transit-like signal associated with the star EPIC 218916923 with both DST and EXOTRANS. As a sanity check, we downloaded the EVEREST light curve of EPIC 218916923 (Luger et al. 2016) and detected the same signal. We note that Vanderburg & Johnson (2014) and Luger et al. (2016) used the same mask to extract the time series data from the raw *K2* images. EPIC 218916923 was proposed for *K2* observations by programmes GO7086 (P.I. Thompson), GO7030 (P.I. Howard), and GO7087 (P.I. Dragomir). We will hereafter refer to the star and its transiting planet as K2-139 and K2-139 b, respectively.

We searched the Vanderburg & Johnson (2014)'s light curve for odd–even transit depth variation and secondary eclipse that might hint to a binary scenario making the system a likely false positive. None of them were significantly detected. The depth of the odd–even transits agrees within the 1σ uncertainty of 1.6×10^{-3}, whereas the 3σ upper limit of the occultation depth is 7.9×10^{-5}, both respect to the normalized flux. We proceeded to more detailed fitting of the light curve, as well as ground-based imaging (Section 3) and spectroscopic observations (Section 4). The main identifiers, coordinates, optical and infrared magnitudes, and proper motions of the star are listed in Table 1. We display the EVEREST *K2* light curve of K2-139 in Fig. 1.

3 ALFOSC IMAGING

K2 Campaign 7 is projected close to the galactic centre and thus in a relatively crowded stellar region. In order to estimate the contamination factor arising from sources whose light leaks into the photometric masks used by Vanderburg & Johnson (2014) and Luger et al. (2016), we observed K2-139 on 2016 September 13 (UT) with the ALFOSC camera mounted at the Nordic Optical Telescope (NOT) of Roque de los Muchachos Observatory (La Palma, Spain). The sky conditions were photometric with excellent seeing conditions (∼0.6 arcsec). We used the Bessel *R* filter and acquired 16 images of 6 s, 2 images of 20 s, and 1 image of 120 s. The data were bias subtracted and flat-fielded using dusk sky flats. Aperture photometry was then performed on all stars within the mask used in the extraction of the light curve by Vanderburg & Johnson (2014) and Luger et al. (2016).

Several fainter stars can be identified inside the photometric mask (Fig. 2), of which the two brightest sources are also in the

[1] Source: http://exoplanet.eu, as of 2017 January.
[2] See http://keplerscience.arc.nasa.gov/k2-fields.html.
[3] Publicly available at https://www.cfa.harvard.edu/avanderb/allk2c7obs.html.

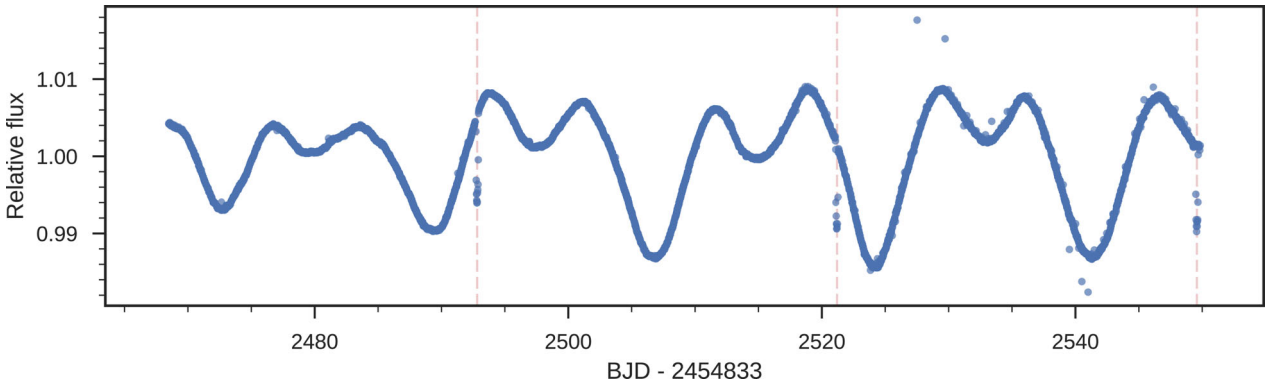

Figure 1. *K2* Light curve for K2-139 as extracted by Luger et al. (2016). The positions of the three observed transits are marked with vertical dashed lines.

Table 1. Main identifiers, coordinates, optical and infrared magnitudes, and proper motion of K2-139.

Parameter	Value	Source
Main identifiers		
TYC	6300-2008-1	*Tycho*
EPIC	218916923	EPIC
UCAC	361-185490	EPIC
2MASS	19161596-1754384	EPIC
Equatorial coordinates		
α(J2000.0)	$19^{h}16^{m}15.967^{s}$	2MASS
δ(J2000.0)	$-17^{\circ}54'38.48''$	2MASS
Magnitudes		
B	12.433 ± 0.205	EPIC
V	11.653 ± 0.137	EPIC
g	12.049 ± 0.010	EPIC
r	11.400 ± 0.010	EPIC
J	10.177 ± 0.022	2MASS
H	9.768 ± 0.022	2MASS
K	9.660 ± 0.023	2MASS
*W*1	9.598 ± 0.024	*WISE*
*W*2	9.684 ± 0.020	*WISE*
*W*3	9.593 ± 0.043	*WISE*
*W*4	8.487	*WISE*
Proper motions		
$\mu_\alpha \cos\delta$ (mas yr^{-1})	38.584 ± 3.907	*Gaia*
μ_δ (mas yr^{-1})	-9.837 ± 3.534	*Gaia*

Note. Values of fields marked with EPIC are taken from the Ecliptic Plane Input Catalog, available at http://archive. stsci.edu/k2/epic/search.php. Values marked with *Gaia*, 2MASS, and *WISE* are from Fabricius et al. (2016), Cutri et al. (2003), and Cutri et al. (2012), respectively. The *WISE W*4 magnitude is an upper limit.

EPIC catalogue with *Kepler* band magnitudes of 16.8 and 18.4. The closest detected source is a 6.8-mag fainter star at 3.8″ south of K2-139. We can exclude stars as faint as ∼20 mag at an angular distance larger than ∼0.6arcsec from K2-139. It is worth noting that the faintest star whose flux could account for the ∼1 per cent deep transit of K2-139 cannot be more than ∼5 mag fainter than our target. The summed flux of these faint stars amounts to 1.4 ± 0.3 per cent of the total off-transit flux within the aperture. We subtracted this contamination flux from the EVEREST *K2* light curve prior to performing the joint analysis presented in Section 6.

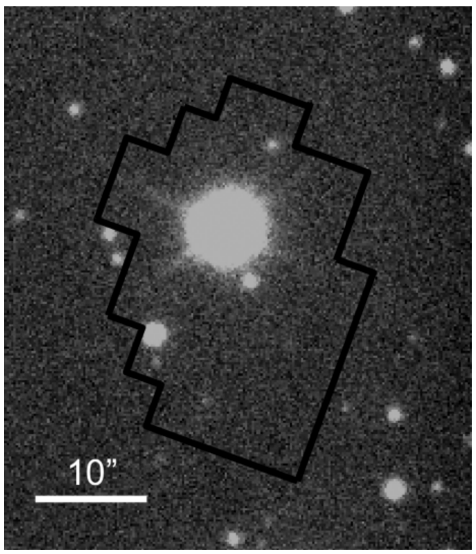

Figure 2. ALFOSC Bessel *R*-band image of the sky region around K2-139. North is up and east is to the left. The target star is the brightest source in the middle. The solid black polygon marks the EVEREST photometric mask (Luger et al. 2016).

4 HIGH-RESOLUTION SPECTROSCOPY

In 2016 June and August, we obtained two reconnaissance spectra of K2-139 with the Tull spectrograph (Tull et al. 1995) at the 2.7-m telescope at McDonald Observatory (Texas, USA). The high-resolution ($R \approx 60\,000$) spectra have a signal-to-noise ratio (S/N) ∼30 per pixel at 5500 Å. We reduced the data using standard `iraf` routines and derived preliminary spectroscopic parameters using our code `Kea` (Endl & Cochran 2016). The results from both spectra are nearly identical and reveal a star with $T_{\rm eff} = 5500 \pm 100$ K, $\log g_\star = 4.65 \pm 0.12$ (cgs), [Fe/H]=$+0.11 \pm 0.12$ dex, and a slow projected rotational velocity of $v \sin i_\star \approx 2$ km s^{-1}.

The high-precision radial velocity follow-up of K2-139 was started in 2016 June with the FIbre-fed Échelle Spectrograph (FIES; Frandsen & Lindberg 1999; Telting et al. 2014) mounted at the 2.56-m NOT. The observations were carried out as part of the OPTICON and CAT observing programs 16A/055, P53-201, and P53-203. We used the *high-resolution* mode, which provides a resolving power of $R \approx 67\,000$ in the whole visible spectral range (3700–7300 Å). The exposure time was set to 2100–3600 s, based on sky conditions and observing scheduling constraints. Following the observing strategy outlined in Buchhave et al. (2010)

Table 2. Radial velocity measurements and activity indexes of K2-139.

BJD_{TDB} −2450 000	RV (km s^{-1})	σ_{RV} (km s^{-1})	CCF BIS (km s^{-1})	CCF FWHM (km s^{-1})	$\log R'_{HK}$	$\sigma_{\log R'_{HK}}$
FIES						
7565.656116	−31.3755	0.0160	0.0119	12.1638	–	–
7568.556388	−31.3503	0.0155	0.0129	12.1080	–	–
7569.567239	−31.3317	0.0153	0.0264	12.1590	–	–
7570.606019	−31.3473	0.0136	0.0098	12.1547	–	–
7572.576513	−31.3357	0.0133	0.0107	12.1226	–	–
7574.529831	−31.3466	0.0101	0.0072	12.1158	–	–
7576.536114	−31.2990	0.0136	0.0016	12.1254	–	–
7579.547224	−31.3441	0.0139	−0.0015	12.1284	–	–
7585.551244	−31.3706	0.0111	0.0084	12.1410	–	–
7589.540362	−31.3913	0.0143	0.0130	12.1236	–	–
HARPS						
7569.714094	−31.1633	0.0032	0.0144	7.4922	−4.552	0.028
7587.830287	−31.2146	0.0052	0.0142	7.4843	−4.578	0.060
7589.523734	−31.2116	0.0049	0.0131	7.5051	−4.596	0.042
7610.717929	−31.2217	0.0028	0.0045	7.4363	−4.588	0.025
7619.531746	−31.2190	0.0031	−0.0146	7.4440	−4.498	0.021
7620.682635	−31.2049	0.0069	0.0069	7.4263	−4.455	0.052
HARPS-N						
7586.621783	−31.2048	0.0029	0.0103	7.4501	−4.461	0.018
7587.603577	−31.2141	0.0038	0.0072	7.4396	−4.476	0.025
7605.429766	−31.1683	0.0050	−0.0003	7.4336	−4.479	0.040

and Gandolfi et al. (2015), we traced the RV drift of the instrument by acquiring long-exposed ($T_{exp} \approx 35$ s) ThAr spectra immediately before and after the target observations. The typical RV drift measured between two ThAr spectra bracketing a 2100–3600 s science exposure is about 50–80 m s^{-1}. A linear interpolation of the RV drift to the mid-time of the science exposure allows us to achieve a radial velocity zero-point stability of about 5–6 m s^{-1}, which is two to three times smaller than the nominal error bars listed in Table 2. The data reduction uses standard `iraf` and `idl` routines. The S/N of the extracted spectra is ∼30–40 per pixel at 5500 Å. Radial velocity measurements were extracted via multi-order cross-correlation with the RV standard star HD 182572, observed with the same instrument set-up as K2-139.

We also observed K2-139 in 2016 July, August, and September with the HARPS (Mayor et al. 2003) and HARPS-N (Cosentino et al. 2012) spectrographs mounted at the ESO 3.6-m Telescope of La Silla Observatory (Chile) and at the 3.58-m Telescopio Nazionale Galileo (TNG) of Roque de los Muchachos observatory (La Palma, Spain), respectively. Both instruments provide a resolving power of $R \approx 115\,000$ in the wavelength range ∼3800–6900 Å. The observations were performed as part of the ESO and TNG observing programs 097.C-0948 and A33TAC_15, respectively. The exposure time was set to 1800 s, leading to an S/N ∼35 on the extracted spectra. We reduced the data using the dedicated HARPS and HARPS-N pipelines and extracted the RVs by cross-correlation with a G2 numerical mask.

The FIES, HARPS, and HARPS-N RVs are listed in Table 2 along with the bisector span (BIS) and the full width at half-maximum (FWHM) of the cross-correlation function (CCF). Time stamps are given in barycentric Julian date in barycentric dynamical time (BJD_{TDB}). For the HARPS and HARPS-N data, we also provide the Ca II H & K chromospheric activity index $\log R'_{HK}$. We did not measure $\log R'_{HK}$ from the FIES spectra because of the poor S/N at wavelengths shorter than 4000 Å.

5 STELLAR PARAMETERS

5.1 Spectral analysis

We derived the spectroscopic parameters of K2-139 from the co-added FIES spectra. The stacked FIES data have an S/N ∼110 per pixel at 5500 Å. We adopted three different methods. For each method, results are reported in Table 3.

First method. The technique fits spectral features that are sensitive to different photospheric parameters. It uses the stellar spectral synthesis program `Spectrum` (Gray 1999) to compute synthetic spectra from `ATLAS 9` model atmospheres (Castelli & Kurucz 2004). Microturbulent (v_{mic}) and macroturbulent (v_{mac}) velocities are derived from the calibration equations of Bruntt et al. (2010) and Doyle et al. (2014). We used the wings of the Hα and Hβ lines to estimate the effective temperature (T_{eff}), and the Mg I 5167, 5173, and 5184 Å, Ca I 6162 and 6439 Å, and the Na I D lines to determine the surface gravity $\log g_\star$. We simultaneously fitted different spectral regions to measure the iron abundance [Fe/H]. The projected rotational velocity $v \sin i_\star$ was determined by fitting the profile of many isolated and unblended metal lines.

Second method. It relies on the use of the spectral analysis package Spectroscopy Made Easy (`SME`; Valenti & Piskunov 1996; Valenti & Fischer 2005). For a set of given stellar parameters, `SME` calculates synthetic spectra and fits them to high-resolution observed spectra using a chi-squared minimization procedure. We used `SME` version 4.4.3 and `ATLAS 12` model spectra (Kurucz 2013). We adopted the same calibration equation as described in the first method to determine v_{mic} and v_{mac}. Effective temperature is derived from the Hα wings; $\log g_\star$ from the Ca I 6102, 6122, 6162, and 6439 Å lines; [Fe/H] and $v \sin i_\star$ from isolated iron lines.

Third method. It uses the classical equivalent width (EW) method adopting the following criteria: (i) T_{eff} is obtained by removing trends between abundance of the chemical elements and the respective excitation potentials; (ii) $\log g_\star$ is optimized by assuming the

Table 3. Spectroscopic parameters of K2-139 as derived using the three methods described in Section 5.

Method	$T_{\rm eff}$ (K)	$\log g_\star$ (cgs)	[Fe/H] (dex)	$v_{\rm mic}$ ($\rm km\,s^{-1}$)	$v_{\rm mac}$ ($\rm km\,s^{-1}$)	$v \sin i_\star$ ($\rm km\,s^{-1}$)
Adopted spectroscopic parameters						
Method 1	5340 ± 110	4.50 ± 0.09	0.22 ± 0.08	0.9 ± 0.1	2.5 ± 0.6	2.8 ± 0.6
Method 2	5185 ± 100	4.53 ± 0.10	0.20 ± 0.10	0.8 ± 0.1	2.4 ± 0.5	3.0 ± 0.5
Method 3	5343 ± 99	4.58 ± 0.21	0.21 ± 0.10	0.9 ± 0.1	–	–

Table 4. Model comparison.

Model	Comment	$N_{\rm pars}$	$K_{\rm b}$ ($\rm m\,s^{-1}$)	χ^2/dof[a]	$\ln \mathcal{L}$	AIC[b]
P0	Planet signal	6	29.1 ± 2.0	6.1	35.6	−60
P1	Planet signal + 1 sine-curve at $P_{\rm rot}$	9	29.4 ± 2.4	3.4	58.1	−98
P2	Planet signal + 2 sine-curves at $P_{\rm rot}$ and $P_{\rm rot}/2$	11	$27.3^{+2.6}_{-2.5}$	3.8	60.1	−98
P3	Planet signal + 3 sine-curves at $P_{\rm rot}$, $P_{\rm rot}/2$, and $P_{\rm rot}/3$	13	$27.8^{+2.7}_{-2.6}$	5.3	59.3	−93
NP1	1 sine curve at $P_{\rm rot}$ (no planet signal)	6	0	18.5	−44.8	101
NP2	2 sine curves at $P_{\rm rot}$ and $P_{\rm rot}/2$ (no planet signal)	8	0	15.9	−12.0	40

[a] χ^2 value assuming no jitter.
[b] We used the Akaike Information Criteria (AIC $= 2N_{\rm pars} - \ln 2\mathcal{L}$) instead of the widely used Bayesian information criteria (BICs) because our RV data sample is small (19 data points), and BICs perform better for large samples (Burnham & Anderson 2002).

ionization equilibrium condition, i.e. by requiring that for a given species, the same abundance (within the uncertainties) is obtained from lines of two ionization states (typically, neutral and singly ionized lines); (iii) $v_{\rm mic}$ is set by minimizing the slope of the relationship between abundance and the logarithm of the reduced EWs. The EWs of Fe I and Fe II lines are measured using the code DOOp (Cantat-Gaudin et al. 2014), a wrapper of DAOSPEC (Stetson & Pancino 2008). The stellar atmosphere parameters are derived with the program FAMA (Magrini et al. 2013), a wrapper of MOOG (Sneden et al. 2012). We used the public version of the atomic data prepared for the *Gaia*-ESO Survey (Heiter et al. 2015) and based on the VALD3 data (Ryabchikova, Pakhomov & Piskunov 2011). We used ∼200 Fe I lines and ∼10 Fe II lines for the determination of the stellar parameters.

The three methods provide consistent results within the 1σ error bars (Table 5). While we have no reason to prefer one technique over the other, we adopted the parameter estimates of the first method, i.e. $T_{\rm eff} = 5340 \pm 110$ K, $\log g_\star = 4.50 \pm 0.09$ (cgs), [Fe/H] $= 0.22 \pm 0.08$ dex, $v_{\rm mic} = 0.9 \pm 0.1 \rm km\,s^{-1}$, $v_{\rm mac} = 2.5 \pm 0.6 \rm km\,s^{-1}$ and $v \sin i_\star = 2.8 \pm 0.6 \rm km\,s^{-1}$. As a sanity check, we also analysed the HARPS and HARPS-N data and obtained consistent results but with larger error bars, owing to the lower S/N of the co-added HARPS and HARPS-N spectra compared to that of the co-added FIES data. Using the Boyajian et al. (2013)'s calibration (see their table 6), the effective temperature of K2-139 defines the spectral type of the host star as K0 V.

5.2 Interstellar extinction

We measured the visual reddening ($A_{\rm V}$) of K2-139 following the technique described in Gandolfi et al. (2008). We fitted the spectral energy distribution of the star to synthetic colours extracted from the BT-NEXTGEN model spectrum (Allard, Homeier & Freytag 2011) with the same photospheric parameters as the star. We adopted the extinction law of Cardelli, Clayton & Mathis (1989) and assumed a normal value for the total-to-selective extinction, i.e. $R_{\rm V} = A_{\rm V}/E(B-V) = 3.1$. We measured a visual extinction of $A_{\rm V} = 0.07 \pm 0.05$ mag. This value is below the upper limit of $A_{\rm V} \lesssim 0.3$ mag extracted from the Schlegel, Finkbeiner & Davis (1998)'s all-sky extinction map, corroborating our result.

5.3 Rotational period

The *K2* light curve of K2-139 displays periodic and quasi-periodic variations with a peak-to-peak photometric amplitude of ∼2 per cent (Fig. 1). The late-type spectral type of the star suggests that the observed variability is due to Sun-like spots appearing and disappearing from the visible stellar disc, as the star rotates around its axis. This is corroborated by the fact that K2-139 is a chromospherically active star. The HARPS and HARPS-N spectra show clear emission components in the cores of the Ca II H&K lines, from which we measured an average activity index of $\log R'_{\rm HK} = -4.46 \pm 0.06$.[4]

The out-of-transit photometric variability observed in the light curve of K2-139 is mainly due to two active regions located at opposite stellar longitudes, whose lifetime is longer than the duration of the *K2* observations. Using the spots as tracers of stellar rotation and following the autocorrelation function (ACF) technique described in McQuillan, Mazeh & Aigrain (2014), we estimated that the rotational period of the star is $P_{\rm rot} = 17.24 \pm 0.12$ d. The Lomb–Scargle periodogram of the light curve shows its strongest peak at the same period confirming our results.

It is worth noting that the rotation period ($P_{\rm rot} = 17.24 \pm 0.12$ d) and radius ($R_\star = 0.862 \pm 0.032\ R_\odot$; see the next section) of the host star translate into a maximum value for the projected rotational velocity of $v \sin i_{\star,\,\rm max} = 2.53 \pm 0.10\ \rm km\,s^{-1}$, which agrees with the spectroscopically derived $v \sin i_\star = 2.8 \pm 0.6\ \rm km\,s^{-1}$, suggesting that the star is seen nearly equator-on ($i_\star \approx 90^\circ$) and that the system might be aligned along the line of sight.

[4] This value is corrected for the interstellar medium absorption, following the procedure described in Fossati et al. (2017) and using the measured stellar parameters and reddening. The correction is +0.06. The star is therefore slightly more active than what measured from the spectra.

Table 5. K2-139 system parameters.

Parameter	Prior[a]	Final value
Stellar parameters		
Star mass $M_\star$ ($M_\odot$)	–	0.919 ± 0.033
Star radius $R_\star$ ($R_\odot$)	–	0.862 ± 0.032
Star density $\rho_\star$ (from spectroscopy, g cm^{-3})	–	$2.02^{+0.25}_{-0.22}$
Star density $\rho_\star$ (from light curve, g cm^{-3})	–	$2.11^{+0.74}_{-0.81}$
Effective temperature $T_{\rm eff}$ (K)	–	5340 ± 110
Surface gravity $\log g_\star$ (cgs)	–	4.50 ± 0.09
Iron abundance [Fe/H] (dex)	–	0.22 ± 0.08
Microturbulent velocity $v_{\rm mic}$ (km s^{-1})	–	0.9 ± 0.1
Macroturbulent velocity $v_{\rm mac}$ (km s^{-1})	–	2.5 ± 0.6
Projected rotational velocity $v \sin i_\star$ (km s^{-1})	–	2.8 ± 0.6
Rotational period $P_{\rm rot}$ (d)	–	17.24 ± 0.12
Activity index[b] $\log R'_{\rm HK}$	–	-4.46 ± 0.06
Gyrochronological age (Gyr)	–	1.8 ± 0.3
Interstellar extinction $A_{\rm V}$ (mag)	–	0.07 ± 0.05
Star distance d (pc)	–	152 ± 10
Model parameters of K2-139 b		
Orbital period $P_{\rm orb}$ (d)	$\mathcal{U}[28.3773, 28.3873]$	28.38236 ± 0.00026
Transit epoch T_0 (BJD$_{\rm TDB}$ −2450 000)	$\mathcal{U}[7325.8120, 7325.8220]$	7325.81714 ± 0.00033
Scaled semimajor axis $a/R_\star$	$\mathcal{U}[1.2, 100]$	$44.8^{+4.7}_{-6.7}$
Planet-to-star radius ratio $R_{\rm p}/R_\star$	$\mathcal{U}[0, 0.2]$	$0.0961^{+0.0023}_{-0.0015}$
Impact parameter, b	$\mathcal{U}[0, 1.2]$	$0.30^{+0.21}_{-0.19}$
$\sqrt{e}\sin\omega$	$\mathcal{U}[-1, 1]^c$	$0.10^{+0.29}_{-0.30}$
$\sqrt{e}\cos\omega$	$\mathcal{U}[-1, 1]^c$	$0.06^{+0.24}_{-0.27}$
Radial velocity semi-amplitude variation K (m s^{-1})	$\mathcal{U}[0, 200]$	$27.7^{+6.0}_{-5.3}$
Model parameters of RV sinusoidal signal at $P_{\rm rot}$		
Period $P_{\rm rot}$ (d)	$\mathcal{N}[17.24, 0.12]$	17.26 ± 0.12
Epoch T_0 (BJD$_{\rm TDB}$ −2 450 000)	$\mathcal{U}[7324.0, 7341.3]$	$7332.4^{+5.5}_{-5.1}$
Radial velocity semi-amplitude variation K (m s^{-1})	$\mathcal{U}[0, 200]$	$7.1^{+7.5}_{-5.0}$
Model parameters of RV sinusoidal signal at $P_{\rm rot}/2$		
Period $P_{\rm orb}$ (d)	$\mathcal{F}[P_{\rm rot}/2]$	8.63 ± 0.06
Epoch T_0 (BJD$_{\rm TDB}$ −2 450 000)	$\mathcal{U}[7317.0, 7325.7]$	7321.3 ± 2.2
Radial velocity semi-amplitude variation K (m s^{-1})	$\mathcal{U}[0, 200]$	$10.6^{+7.7}_{-6.9}$
Additional model parameters		
Parametrized limb-darkening coefficient q_1	$\mathcal{U}[0, 1]$	$0.37^{+0.18}_{-0.13}$
Parametrized limb-darkening coefficient q_2	$\mathcal{U}[0, 1]$	$0.48^{+0.24}_{-0.16}$
Systemic velocity $\gamma_{\rm FIES}$ (km s^{-1})	$\mathcal{U}[-32.3913, -30.2990]$	-31.3575 ± 0.0064
Systemic velocity $\gamma_{\rm HARPS}$ (km s^{-1})	$\mathcal{U}[-32.2217, -30.1633]$	-31.1970 ± 0.0093
Systemic velocity $\gamma_{\rm HARPS\text{-}N}$ (km s^{-1})	$\mathcal{U}[-32.2141, -30.1683]$	$-31.1950^{+0.0122}_{-0.0128}$
Jitter term $\sigma_{\rm FIES}$ (m s^{-1})	$\mathcal{U}[0, 100]$	$9.6^{+9.8}_{-6.5}$
Jitter term $\sigma_{\rm HARPS}$ (m s^{-1})	$\mathcal{U}[0, 100]$	$15.4^{+11.0}_{-7.6}$
Jitter term $\sigma_{\rm HARPS\text{-}N}$ (m s^{-1})	$\mathcal{U}[0, 100]$	$10.2^{+15.8}_{-7.3}$
Derived parameters of K2-139 b		
Planet mass $M_{\rm p}$ ($M_{\rm Jup}$)	–	$0.387^{+0.083}_{-0.075}$
Planet radius $R_{\rm p}$ ($R_{\rm Jup}$)	–	$0.808^{+0.034}_{-0.033}$
Planet mean density $\rho_{\rm p}$ (g cm^{-3})	–	$0.91^{+0.24}_{-0.20}$
Semimajor axis of the planetary orbit a (au)	–	$0.179^{+0.021}_{-0.027}$
Orbit eccentricity e	–	$0.12^{+0.12}_{-0.08}$
Argument of periastron of stellar orbit $\omega_\star$ (deg)	–	124^{+175}_{-79}
Orbit inclination $i_{\rm p}$ (deg)	–	$89.62^{+0.25}_{-0.36}$
Transit duration τ_{14} (h)	–	$4.89^{+0.08}_{-0.22}$
Equilibrium temperature[d] $T_{\rm eq}$ (K)	–	565^{+48}_{-32}

Notes. The adopted Sun and Jupiter units follow the recommendations from the International Astronomical Union (Prša et al. 2016).
[a]$\mathcal{U}[a, b]$ refers to uniform priors between a and b, $\mathcal{N}[a, b]$ means Gaussian priors with mean a and standard deviation b and $\mathcal{F}[a]$ to a fixed a value.
[b]Corrected for interstellar reddening following Fossati et al. (2017). The correction is +0.06.
[c]The code always ensures that $e < 1$.
[d]Assuming albedo = 0.

5.4 Stellar mass, radius, and age

We derived the stellar mass, radius, and age using the online interface for Bayesian estimation of stellar parameters available at the following web page: http://stev.oapd.inaf.it/cgi-bin/param. Briefly, the web tool interpolates on to PARSEC model isochrones (Bressan et al. 2012), the *V*-band apparent magnitude, effective temperature, metal content, and parallax. We used the v-band magnitude reported in Table 1 – after correcting for interstellar reddening (Section 5.2) – along with the effective temperature and metal content we derived in Section 5. The parallax was retrieved from the *Gaia*'s first data release (px = 6.56 ± 0.43 mas, $d = 152 \pm 10$ pc; Fabricius et al. 2016). We adopted the lognormal initial mass function from Chabrier (2001).

K2-139 has a mass of $M_\star = 0.919 \pm 0.033\ M_\odot$ and radius of $R_\star = 0.862 \pm 0.032\ R_\odot$, corresponding to a surface gravity of $\log g_\star = 4.503 \pm 0.035$ (cgs), in excellent agreement with the spectroscopically derived value of $\log g_\star = 4.50 \pm 0.09$ (cgs; see Section 5). The derived mean density $\rho_\star = 2.02 \pm 0.24$ g cm^{-3} of K2-139 is also consistent within 1σ with the density estimated by the modelling of the transit light curve ($\rho_\star = 2.11^{+0.74}_{-0.81}$ g cm^{-3}; see Section 6).

The isochrones provide an age of 3.6 ± 3.4 Gyr for K2-139. Using the equations given in Barnes & Kim (2010) and Barnes (2010), the rotation period of 17.3 d (Section 5.3) implies a gyrochronological age of 1.8 ± 0.3 Gyr.

6 JOINT RV-TRANSIT FIT

We performed the joint fit to the photometric and RV data using the code pyaneti[5] (Barragán, Gandolfi & Antoniciello 2017), a PYTHON/FORTRAN software suite based on Markov Chain Monte Carlo (MCMC) methods.

The photometric data included in the joint analysis are subsets of the whole EVEREST *K2* light curve. We used the EVEREST light curve because it provides a slightly better rms over the Vanderburg & Johnson (2014)'s data. We selected ∼10 h of data points around each of the three transits, which have a duration of ∼5 h. We de-trended each individual transits with the code exotrending[6] (Barragán & Gandolfi 2017), using a second-order polynomial fitted to the out-of-transit points. The fitted data include 12 points immediately before and after each transit, with the exception of the last transit for which only 9 data points are available. We removed the data points that are affected by stellar spot crossing events (see Section 7.1 for more details).

We fitted the RV data using a Keplerian model for the planet, along with two sine-like curves to account for the activity-induced RV (see the next section for details). We adopted the limb-darkened quadratic law of Mandel & Agol (2002) for the transit model. We adopted the Gaussian likelihood

$$\mathcal{L} = \left[\prod_{i=1}^{n} \left\{2\pi \left(\sigma_i^2 + \sigma_j^2\right)\right\}^{-1/2}\right] \exp\left\{-\sum_{i=1}^{n} \frac{1}{2} \frac{(D_i - M_i)^2}{\sigma_i^2 + \sigma_j^2}\right\}, \quad (1)$$

where n is the number of data points, σ_i is the error associated with each data point D_i, M_i is the model associated with a given D_i and σ_j is an extra noise term, sometime referred as jitter.

The sampling method and fitted parameters are the same as in Barragán et al. (2016). Details on the adopted priors are given in Table 5. Following Kipping (2010), we super-sampled the light curve model using 10 subsamples per *K2* exposure to account for the long-cadence acquisition. The parameter space was explored with 500 independent chains created randomly inside the prior ranges. The chain convergence was analysed using the Gelman–Rubin statistics. The burn-in phase uses 25 000 more iterations with a thin factor of 50. The posterior distribution of each parameter has 250 000 independent data points.

7 RESULTS AND DISCUSSION

7.1 Stellar activity modelling

A simple Keplerian model provides a poor fit to the RV measurements with $\chi^2/\mathrm{dof} = 6.1$ (Table 4), suggesting that additional signals might be present in our Doppler data. Activity-induced RV variation is expected given the 2 per cent peak-to-peak photometric variability observed in the *K2* light curve of K2-139 (Fig. 1) and the Ca II H & K activity index of $\log R'_{\mathrm{HK}} = -4.46 \pm 0.06$ (Section 5.3). The *K2* photometric variation corresponds to a spot filling factor of approximately 2 per cent, if this variation is due to cool starspots. We can use the empirical relationship relating spot coverage to RV amplitude from Saar & Donahue (1997) or Hatzes (2002) to estimate the RV amplitude expected from spots. Using the projected rotational velocity of 2.8 km s^{-1} results in an RV semi-amplitude of ≈20–30m s^{-1}. The code SOAP 2, designed to estimate the effect of active regions on photometric and spectroscopic measurements (Dumusque, Boisse & Santos 2014), provides consistent results.

In order to look for additional signals in our Doppler data, we performed a frequency analysis of the RV measurements and activity indicators. On one occasion[7] K2-139 was observed with FIES and HARPS-S nearly simultaneously (within less than 25 min). We used the two sets of measurements to estimate the RV, FWHM, and BIS offsets between the two instruments. We assumed no offset between HARPS-N and HARPS. While we acknowledge that this assumption is arbitrary, we note that the modelling of the RV data gives an offset of $\Delta\,\mathrm{RV}_{(\mathrm{HN\text{-}H})} = 0.0020 \pm 0.0093$km s^{-1} (Table 5), which is consistent with zero.

Fig. 3 displays the generalized Lomb–Scargle periodograms (Zechmeister & Kürster 2009) of the combined data sets. From top to bottom, it displays the RV data (first panel), the RV residuals after subtracting the transiting planet signal (second panel), the BIS (third panel), and FWHM (fourth panel) of the CCF. The periodogram of the window function is shown in the lower panel. The dotted vertical blue lines mark the frequency at the orbital period of the planet (0.035 c/d), as well as the frequencies at the rotation period of the star (0.058 c/d) and its first two harmonics (0.116 and 0.174 c/d).

The periodogram of the RV data (upper panel) shows a peak at the orbital frequency of the planet along with two additional peaks at 0.095 and 0.130 c/d. Since the periodogram of the window function shows two peaks at ∼0.060 and ∼0.095 c/d (lower panel, red arrows), we interpreted the 0.095 and 0.130 c/d peaks as the aliases of the orbital frequency.[8] We note also that periodogram of the BIS of the CCF displays peaks whose frequencies

[5] Available at https://github.com/oscaribv/pyaneti.
[6] Available at https://github.com/oscaribv/exotrending.
[7] Epoch BJD=2457589.
[8] 0.095 = 0.035 + 0.060 c/d and 0.130 = 0.035 + 0.095 c/d.

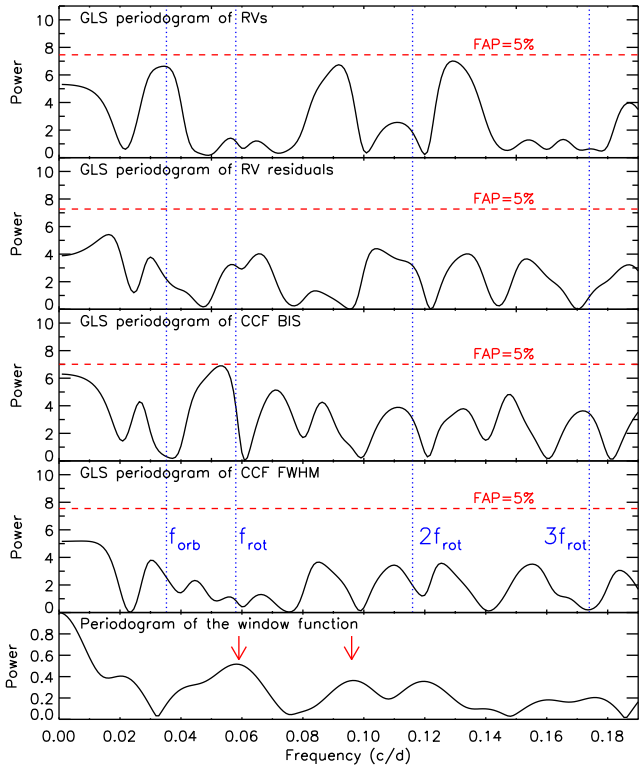

Figure 3. Generalized Lomb–Scargle periodogram of the combined FIES, HARPS, and HARPS-N Doppler data sets. From top to bottom: the RV data, the RV residuals after subtracting the transiting planet signal, the BIS and FWHM of the CCF, and the window function. The dotted vertical blue lines mark the frequencies at the orbital period, as well as at the stellar rotation period and its first two harmonics. The dashed horizontal red lines mark the 5 per cent FAPs as derived using the bootstrap method. The red arrows in the lower panel mark the two peaks presented in the main text.

are close to the stellar rotation frequency and its first two harmonics. However, none of the peaks visible in the GLS periodograms of Fig. 3 has a false alarm probability (FAP)[9] lower than 5 per cent. Although our spectroscopic data show neither additional signals, we note that the semi-amplitude variation of the BIS and FWHM is expected to be $\lesssim$10–15 m s^{-1} (Dumusque et al. 2014), which is comparable with the uncertainties of most of our measurements (Table 2). The lack of significant peaks in the periodogram of the RV data and RV residuals, as well as in the periodogram of the activity indicators, could be explained by the limited number of available measurements and their uncertainties. We conclude that we cannot exclude the existence of spot-induced signals in our RV measurements.

Photometric and radial velocity variations due to rotational modulation can be complex with not only the rotational period $P_{\rm rot}$ present but also its harmonics, e.g. $P_{\rm rot}/2$ and $P_{\rm rot}/3$. Assuming that the surface structures responsible for this modulation (e.g. cool spots) are not evolving rapidly, then the simplest representation of the rotational modulation is through the Fourier components defined by the rotation period and its harmonics. Fig. 1 shows that the evolution time-scale of the active regions in the stellar surface is longer than the 80-d duration of the *K2* campaign. Since our RV follow-up spans 55 d, we can assume that any activity-induced RV signal is coherent within our observing window. This approach has been used previously for other planetary systems orbiting active stars (e.g. Pepe et al. 2013).

The Fourier analysis of the *K2* light curve is the best way to measure the contribution of the rotation period and its harmonics to the quasi-periodic photometric variability of the star. We therefore analysed the *K2* light curve using a pre-whitening procedure. That is, the dominant period was found, a sine-fit made to the data and subtracted, and additional periods searched in the residual data. We used the program `Period04` (Lenz & Breger 2005) for this procedure.

The dominant periods are ∼17.2 d, i.e. the rotation period of the star (Section 5.3), and roughly the first four harmonics (i.e. 8.6, 5.7, 4.3, and 3.4 d). The 17.2- and 8.6-d periods have about the same amplitude, while the 5.7-d period ($P_{\rm rot}/3$) has 10 per cent of the main amplitude. The $P_{\rm rot}/4$ signal has only about 4 per cent of the main amplitude. The light-curve analysis indicates that the signal due to rotational modulation can largely be represented by the rotational period ($P_{\rm rot}$) and its first harmonic ($P_{\rm rot}/2$).

In order to test if the addition of RV sinusoidal signals at the stellar rotation period and its harmonics can account for the additional variation seen in our RV measurements, we compared different models by adding signals one by one. The first model (P0) includes only the planet signal, i.e. a Keplerian model fitted to the RV data using the same priors given in Table 5, but fixing epoch and period to the values derived by the transit modelling. The next model (P1) is obtained from P0 by adding a sinusoidal signal at the rotation period of the star ($P_{\rm rot}$). Models P2 includes the first harmonic of the rotation period ($P_{\rm rot}/2$), whereas model P3 account for the first ($P_{\rm rot}/2$) and second ($P_{\rm rot}/3$) harmonics. While adding sinusoidal signals, we fitted for their amplitudes, phases, and periods. We used flat priors for the phases and amplitudes (details in Table 5). We used a Gaussian prior for $P_{\rm rot}$ using the value and its uncertainty derived in Section 5.3. The periods of the harmonic signals were left free to vary depending on the value assumed by $P_{\rm rot}$ at each step of the MCMC chains. In order to check if the RV variation induced by the planet is significant in our data set, we also performed the fit using models where the planetary signal was not included (models NP1 and NP2; see Table 4).

Table 4 shows the goodness of the fit for each model. The preferred model is P2 (planet plus 2 sinusoidal signals at $P_{\rm rot}$ and $P_{\rm rot}/2$) with the lowest Akaike Information Criteria (AIC) and maximum likelihood. This result is consistent with the Fourier analysis of the *K2* light curve, which suggests that the major contribution to the photometric variations arises from the stellar rotation period and its first harmonic. Our analysis provides also additional evidence that the Doppler motion induced by the planet is present in our RV data set. First, the planet signal does not significantly vary for the P0, P1, P2, and P3 models (Table 4). Secondly, the models with no planetary signal (NP1 and NP2) provide a poor fit to the RV measurements (Table 4).

To account for additional instrumental noise not included in the nominal RV error bars and/or imperfect treatment of the various sources of RV variations, we fitted for a jitter term for each instrument. The final parameter estimates and their error bars are listed in Table 5. They are defined as the median and the 68 per cent credible interval of the final posterior distributions. The best-fitting transit and RV models are displayed in Fig. 4 along with the photometric and RV data points.

[9] We determined the FAP following the Monte Carlo bootstrap method described in Kuerster et al. (1997).

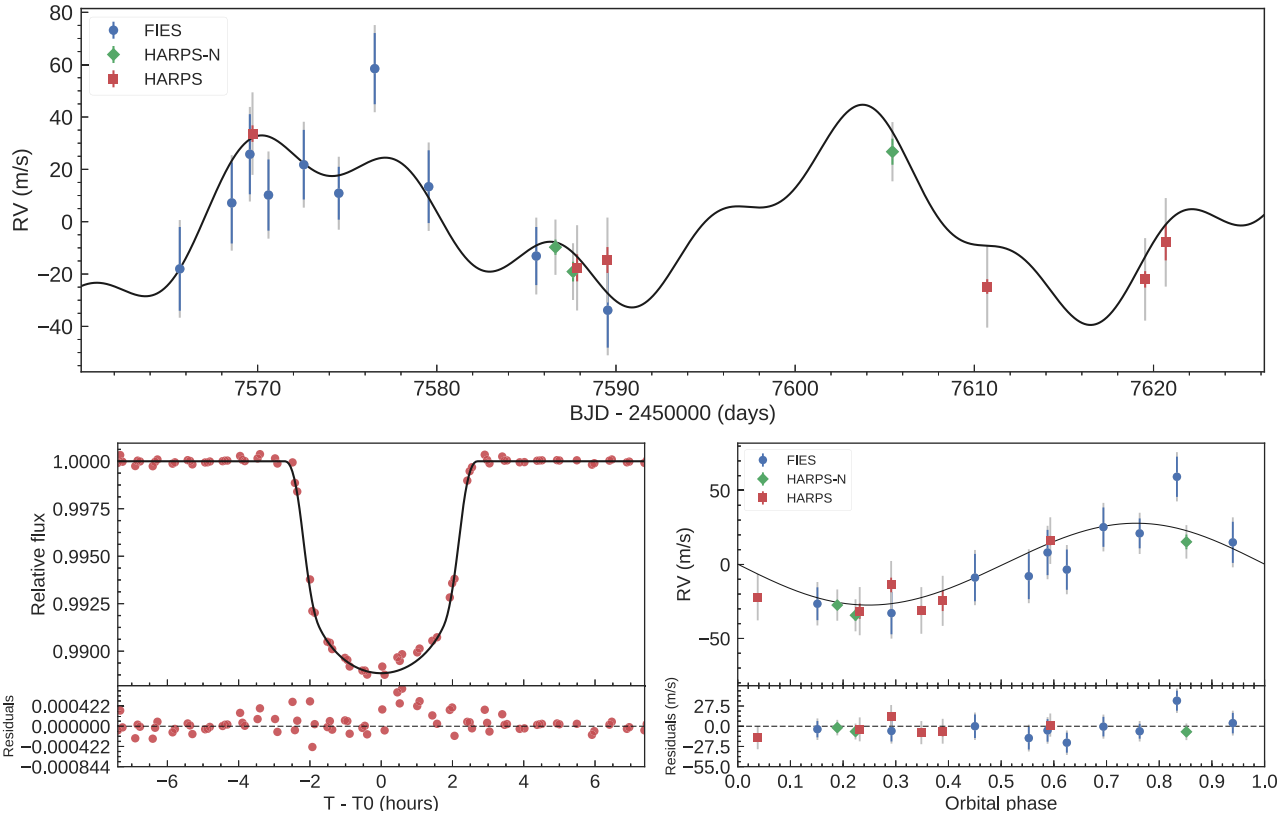

Figure 4. Top: FIES (blue circles), HARPS-N (green diamonds) and HARPS (red squares) RV measurements *versus* time, following the subtraction of the systemic velocities for each instrument. The 1σ uncertainties are marked using the same colour used for each data set. The vertical grey lines mark the error bars including jitter. The solid line represents the best-fitting RV model, which includes the planet signal, and the activity signal at the stellar rotation period and its first harmonic. The dashed, dash–dotted, and dotted lines show the RV contribution of K2-139 b, stellar rotation, and first harmonic, respectively. Lower left-hand panel: Transit light curve folded to the orbital period of K2-139 b and residuals. The red points mark the *K2* data and their error bars. The solid line mark the re-binned best-fitting transit model. Lower right-hand panel: Phase-folded RV curve of K2-139 b and best-fitting Keplerian solution (solid line), following the subtraction of the two additional sinusoidal signals used to account for the stellar activity. The FIES, HARPS, and HARPS-N are corrected for the instrument offsets as derived from the global analysis.

7.2 Additional companion

Huang et al. (2016) found that warm Jupiters with low eccentricities ($e \lesssim 0.4$) have inner low-mass companions. They used this evidence as an argument in favour of the *in situ* formation, since the planet migration would have cleaned the warm Jupiter neighbourhood. We searched the light curve for additional transit signals but found no evidence for an additional transiting planet in the system. As described in the previous paragraph, the periodogram of the RV residuals show no significant peak with FAP lower than 5 per cent.

7.3 Spot-crossing events

The passage of a planet in front of a spot can be detected as a bump in the transit light curve (see e.g. Sanchis-Ojeda & Winn 2011). Spot-crossings events are clearly visible in the EVEREST transit light curves (Fig. 4). The same features appear at the same times and with consistent amplitudes in the Vanderburg & Johnson (2014) data, confirming that the bumps are real and not due to systematics. To assess whether the bumps significantly affect the parameter estimates, we performed the joint analysis as described in Section 6 including all the transit data points. We found that the final parameters are consistent within 1σ with those reported in Table 5.

7.4 Planet's composition and formation scenario

With a mass of $M_{\rm p} = 0.387^{+0.083}_{-0.075}\,M_{\rm J}$ and radius of $R_{\rm p} = 0.808^{+0.034}_{-0.033}\,R_{\rm J}$ (resulting in a mean density of $\rho_{\rm p}$=$0.91^{+0.24}_{-0.20}$ g cm^{-3}), K2-139 b joins the small group of well-characterized warm Jupiters. Fig. 5 shows the position of K2-139 b in the mass–radius diagram for warm Jupiters ($M_{\rm p} \geq 0.3\,M_{\rm Jup}$; $10 \leq P_{\rm orb} \leq 100$ d) whose mass and radius have been determined with a precision better than 25 per cent (14 objects). Notably, K2-139 b is the transiting warm Jupiter with the lowest mass known to date, if the definition of giant planets given by Hatzes & Rauer (2015) is adopted. Fig. 5 displays also the planetary models of Fortney, Marley & Barnes (2007) for different core masses and age between 1.0 and 4.5 Gyr. The planet radius of K2-139 b can be explained if the planet has a core[10] of $49^{+19}_{-17}\,M_\oplus$, containing ~40 per cent of the total planetary mass. We expect that K2-139 b has a solid core surrounded by a gaseous envelope.

Rafikov (2006) found that a core of mass 5–20 $M_\oplus$ at a semimajor axis between 0.1 and 1.0 au would be able to start the runaway accretion phase to form a gas-giant planet *in situ*. However, according to his models, these kind of cores are unlikely to form, owing to the high irradiation coming from the star. Boley et al. (2016) suggested instead that more massive cores ($M_{\rm core} \gtrsim 20\,M_\oplus$) can be

[10] Calculated by interpolating Fortney et al. (2007)'s models.

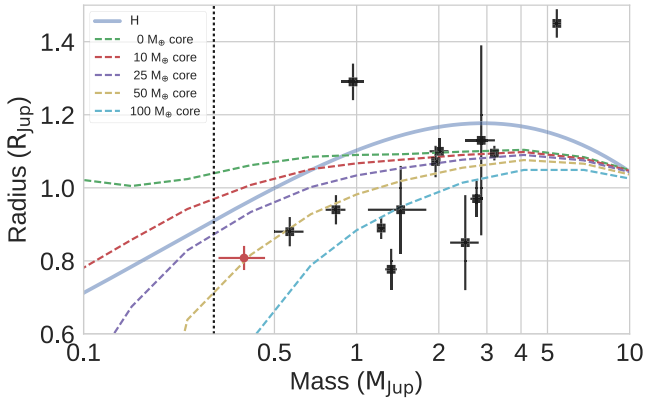

Figure 5. Warm Jupiters (black squares; $M_p \geq 0.3\ M_{Jup}$ and $10 \leq P_{orb} \leq 100$ d) whose mass and radius have been estimated with a precision of at least 25 per cent (as of 2017 January, exoplanet.eu). K2-139 b is shown with a filled red circle. The solid line corresponds to a planet with a pure hydrogen composition (Seager et al. 2007). The dashed lines represent the Fortney et al. (2007) models for planet core masses of 0, 10, 25, 50, and 100 $M_\oplus$. The vertical dotted line marks the giant planet lower limit as defined by Hatzes & Rauer (2015).

built up from the merging of tightly packed inner planets formed at the early stages of the circumstellar disc. Batygin, Bodenheimer & Laughlin (2016) found a similar result and argued that the massive core of HD 149026b ($M_{core} \approx 100\ M_\oplus$) could be explained by one or more super-Earths that merged and accreted the surrounding gas to form a gas-giant planet. Huang et al. (2016) suggested that these cores can initiate runaway accretion if they are formed in a region with enough gas around them, while those without enough volatiles remain super-Earths and represent the population of massive rocky planets unveiled by *Kepler* around solar-like stars (e.g. Demory 2014). Based on these studies and given the semimajor axis of $0.179^{+0.021}_{-0.027}$ au, the $48 \pm 14\ M_\oplus$ core of K2-139 b could have formed the planet *in situ*. We note that the metallicity of K2-139 is relatively high ([Fe/H] $=0.21 \pm 0.05$), suggesting that the primordial circumstellar disc had a relatively high content of dust, which would have enhanced the formation of the core of K2-139 b (see e.g. Johnson & Li 2012). Alternatively, the planet might have formed beyond the snow line and migrated inwards via planet–disc interaction (see e.g. Baruteau et al. 2014).

8 CONCLUSIONS

We confirmed the planetary nature and derived the orbital and main physical parameters of K2-139 b, a warm Jupiter ($T_{eq} = 565^{+48}_{-32}$ K) transiting an active (log $R'_{HK} = -4.46 \pm 0.06$) K0 V star every 29 d. We measured a planetary mass of $M_p = 0.387^{+0.083}_{-0.075}\ M_J$ and radius of $R_p = 0.808^{+0.034}_{-0.033}\ R_J$. At a separation of $a_p = 0.179^{+0.021}_{-0.027}$ au, the mean density of $\rho_p = 0.91^{+0.24}_{-0.20}$ g cm^{-3} implies that the planet has a core of $49^{+19}_{-17}\ M_\oplus$ according to the evolutionary models of Fortney et al. (2007). K2-139 b joins the small group of well-characterized warm Jupiters whose mass and radius have been determined with a precision better than 25 per cent.

The spin-orbit angle, i.e. the angle between the spin axis of the star and the angular momentum vector of the orbit, can provide us with valuable information on the migration mechanisms of exoplanets (see e.g. Winn 2010; Morton & Johnson 2011; Albrecht et al. 2012; Gandolfi et al. 2012). Currently, there are only four warm Jupiters ($M_p \geq 0.3\ M_{Jup}$ and $10 \leq P_{orb} \leq 100$ d) with measured obliquity.[11] From this perspective, K2-139 is an ideal target to measure the sky-project spin-orbit angle via observations of the Rossiter–McLaughlin (RM) effect. Assuming spin-orbit alignment, the expected amplitude of the RM anomaly is $\Delta RV \approx \sqrt{1-b^2}\,(R_p/R_\star)^2\, v \sin i_\star \approx 25$ m s^{-1} (Winn 2010). Given the brightness of the host star ($V = 11.653$ mag), this amplitude can easily be measured using state-of-the-art spectrographs such as HARPS@ESO-3.6m. Moreover, the transit duration (~5 h) is shorter than the visibility of K2-139, which is ~9 h from La Silla observatory (altitude higher than 30° above the horizon).

Alternatively, the spin-orbit angle could be measured from the analysis of the spot-crossing events as described in Sanchis-Ojeda et al. (2011) and Sanchis-Ojeda et al. (2012). Anomalies ascribable to the passage of K2-139 b in front of stellar spots are visible in the three transit light curves observed by *K2*. Unfortunately, the limited number of transits and the *K2* long-cadence data do not allow us to perform a meaningful quantitative analysis of the spot-crossing events. Given the amplitude of the detected anomalies (~0.1 per cent), space-based high-precision photometry is needed to detect the spot-crossing events. Observations performed with the upcoming CHaracterising ExOPlanets Satellite (CHEOPS; Broeg et al. 2013) would allow us to photometrically determine the spin-orbit angle of this system.

ACKNOWLEDGEMENTS

We warmly thank the NOT, ESO, TNG staff members for their unique support during the observations. We are very thankful to Xavier Bonfils, François Bouchy, Martin Kürster, Tsevi Mazeh, Jorge Melendez, and Nuno Santos who kindly agreed to exchange HARPS and FIES time with us. Special thanks go to Antonino Lanza for assisting us with the calculation of the gyro-age of the star. We also greatly thank the anonymous referee for her/his careful review and suggestions, which helped us to improve the manuscript. D.G. gratefully acknowledges the financial support of the *Programma Giovani Ricercatori – Rita Levi Montalcini – Rientro dei Cervelli (2012)* awarded by the Italian Ministry of Education, Universities and Research (MIUR). S.C. thanks the Hungarian OTKA Grant K113117. H. J.D. and D.N. acknowledge support by grant ESP2015-65712-C5-4-R of the Spanish Secretary of State for R& D&i (MINECO). D.L.-O. acknowledges the support from FAPESP (2016/20667-8). This research was supported by the Ministerio de Economia y Competitividad under project FIS2012-31079. The research leading to these results has received funding from the European Union Seventh Framework Programme (FP7/2013-2016) under grant agreement No. 312430 (OPTICON). Based on observations obtained (a) with the NOT, operated on the island of La Palma jointly by Denmark, Finland, Iceland, Norway, and Sweden, in the Spanish Observatorio del Roque de los Muchachos (ORM) of the Instituto de Astrofísica de Canarias (IAC); (b) with the Italian Telescopio Nazionale Galileo (TNG) also operated at the ORM (IAC) on the island of La Palma by the INAF – Fundación Galileo Galilei; (c) the 3.6m ESO telescope at La Silla Observatory under programme ID 097.C-0948. The data presented here were obtained in part with ALFOSC, which is provided by the Instituto de Astrofisica de Andalucia (IAA) under a joint agreement with the University of Copenhagen and NOTSA. This paper includes data collected by the *Kepler* mission. Funding

[11] Source: http://www2.mps.mpg.de/homes/heller/content/main_HRM.html, as of January 2017.

for the *Kepler* mission is provided by the NASA Science Mission directorate. Some of the data presented in this paper were obtained from the Mikulski Archive for Space Telescopes (MAST). STScI is operated by the Association of Universities for Research in Astronomy, Inc., under NASA contract NAS5-26555. Support for MAST for non-*HST* data is provided by the NASA Office of Space Science via grant NNX09AF08G and by other grants and contracts. M.F. and C.M.P. acknowledge generous support from the Swedish National Space Board. C.E. and I.R. are supported by Spanish grant AYA2014-55840-P. P.D. acknowledge the support from INAF and Ministero dell'Istruzione, dell'Università e della Ricerca (MIUR) in the form of the grant 'Premiale VLT 2012' and 'The Chemical and Dynamical Evolution of the Milky Way and Local Group Galaxies'. This work has made use of data from the European Space Agency (ESA) mission *Gaia* (http://www.cosmos.esa.int/gaia), processed by the *Gaia* Data Processing and Analysis Consortium (DPAC; http://www.cosmos.esa.int/web/gaia/dpac/consortium). Funding for the DPAC has been provided by national institutions, in particular the institutions participating in the *Gaia* Multilateral Agreement.

REFERENCES

Albrecht S. et al., 2012, ApJ, 757, 18
Allard F., Homeier D., Freytag B., 2011, in Johns-Krull C., Browning M. K., West A. A., eds, ASP Conf. Ser. Vol. 448, 16th Cambridge Workshop on Cool Stars, Stellar Systems, and the Sun. Astron. Soc. Pac., San Francisco, p. 91
Antonini F., Hamers A. S., Lithwick Y., 2016, ApJ, 152, 174
Barnes S. A., 2010, ApJ, 722, 222
Barnes S. A., Kim Y.-C., 2010, ApJ, 721, 675
Barragán O., Gandolfi D., 2017, Astrophysics Source Code Library, record ascl:1706.001
Barragán O. et al., 2016, AJ, 152, 193
Barragán O., Gandolfi D., Antoniciello G., 2017, Astrophysics Source Code Library, record ascl:1707.003
Baruteau C. et al., 2014, Protostars and Planets VI. p. 667
Batygin K., Bodenheimer P. H., Laughlin G. P., 2016, ApJ, 829, 114
Boley A. C., Granados Contreras A. P., Gladman B., 2016, ApJ, 817, L17
Boyajian T. S. et al., 2013, ApJ, 771, 40
Brahm R. et al., 2016, AJ, 151, 89
Bressan A., Marigo P., Girardi L., Salasnich B., Dal Cero C., Rubele S., Nanni A., 2012, MNRAS, 427, 127
Broeg C. et al., 2013, in Saglia R., ed., EPJ Web Conf. Vol. 47, Hot Planets and Cool Stars. Garching, Germany, p. 03005
Bruntt H. et al., 2010, MNRAS, 405, 1907
Buchhave L. A. et al., 2010, ApJ, 720, 1118
Burnham K., Anderson D., 2002, Model Selection and Multimodel Inference: A Practical Information-Theoretic Approach. Springer-Verlag, New York
Cabrera J. et al., 2009, A&A, 506, 501
Cabrera J., Csizmadia S., Erikson A., Rauer H., Kirste S., 2012, A&A, 548, A44
Cabrera J. et al., 2014, ApJ, 781, 18
Cantat-Gaudin T. et al., 2014, A&A, 562, A10
Cardelli J. A., Clayton G. C., Mathis J. S., 1989, ApJ, 345, 245
Carone L. et al., 2012, A&A, 538, A112
Carpano S. et al., 2009, A&A, 506, 491
Castelli F., Kurucz R. L., 2004, preprint (arXiv:astro-ph/0405087)
Cavarroc C. et al., 2012, Ap&SS, 337, 511
Chabrier G., 2001, ApJ, 554, 1274
Cosentino R. et al., 2012, Proc. SPIE Conf. Ser. Vol. 8446, Ground-based and Airborne Instrumentation for Astronomy IV. SPIE, Bellingham, p. 84461V
Cutri R. M. et al., 2003, 2MASS All Sky Catalog of point sources.
Cutri R. M. et al., 2012, Technical report, Explanatory Supplement to the WISE All-Sky Data Release Products
da Silva R. et al., 2007, A&A, 473, 323
Dawson R. I., Johnson J. A., Morton T. D., Crepp J. R., Fabrycky D. C., Murray-Clay R. A., Howard A. W., 2012, ApJ, 761, 163
Deeg H. J. et al., 2010, Nature, 464, 384
Demory B.-O., 2014, ApJ, 789, L20
Dong S., Katz B., Socrates A., 2014, ApJ, 781, L5
Doyle A. P., Davies G. R., Smalley B., Chaplin W. J., Elsworth Y., 2014, MNRAS, 444, 3592
Dumusque X., Boisse I., Santos N. C., 2014, ApJ, 796, 132
Endl M., Cochran W. D., 2016, PASP, 128, 094502
Erikson A. et al., 2012, A&A, 539, A14
Fabricius C. et al., 2016, A&A, 595, A3
Fortney J. J., Marley M. S., Barnes J. W., 2007, ApJ, 659, 1661
Fossati et al. 2017, A&A, submitted
Frandsen S., Lindberg B., 1999, in Karttunen H., Piirola V., eds, Astrophysics with the NOT. p. 71
Frewen S. F. N., Hansen B. M. S., 2016, MNRAS, 455, 1538
Gandolfi D. et al., 2008, ApJ, 687, 1303
Gandolfi D. et al., 2012, A&A, 543, L5
Gandolfi D. et al., 2015, A&A, 576, A11
Gray R. O., 1999, Astrophysics Source Code Library, record ascl:9910.002
Grziwa S., Pätzold M., 2016, preprint (arXiv:1607.08417)
Grziwa S., Pätzold M., Carone L., 2012, MNRAS, 420, 1045
Hamers A. S., Antonini F., Lithwick Y., Perets H. B., Portegies Zwart S. F., 2016, MNRAS, 464, 688
Hatzes A. P., 2002, Astronomische Nachrichten, 323, 392
Hatzes A. P., Rauer H., 2015, ApJ, 810, L25
Heiter U. et al., 2015, Phys. Scr, 90, 054010
Huang C., Wu Y., Triaud A. H. M. J., 2016, ApJ, 825, 98
Jenkins J. S. et al., 2017, MNRAS, 466, 443
Johnson J. L., Li H., 2012, ApJ, 751, 81
Kipping D. M., 2010, MNRAS, 408, 1758
Kley W., Nelson R. P., 2012, ARA&A, 50, 211
Kovács G., Zucker S., Mazeh T., 2002, A&A, 391, 369
Kuerster M., Schmitt J. H. M. M., Cutispoto G., Dennerl K., 1997, A&A, 320, 831
Kurucz R. L., 2013, Astrophysics Source Code Library, record ascl:1303.024
Lenz P., Breger M., 2005, Commun. Asteroseismol., 146, 53
Luger R., Agol E., Kruse E., Barnes R., Becker A., Foreman-Mackey D., Deming D., 2016, AJ, 152, 100
Magrini L. et al., 2013, A&A, 558, A38
Mandel K., Agol E., 2002, ApJ, 580, L171
Mayor M. et al., 2003, Messenger, 114, 20
McQuillan A., Mazeh T., Aigrain S., 2014, ApJS, 211, 24
Morton T. D., Johnson J. A., 2011, ApJ, 729, 138
Niedzielski A. et al., 2016, A&A, 589, L1
Ortiz M. et al., 2015, A&A, 573, L6
Pepe F. et al., 2013, Nature, 503, 377
Petrovich C., Tremaine S., 2016, ApJ, 829, 132
Prša A. et al., 2016, AJ, 152, 41
Rafikov R. R., 2006, ApJ, 648, 666
Ryabchikova T. A., Pakhomov Y. V., Piskunov N. E., 2011, Kazan Izdatel Kazanskogo Universiteta, 153, 61
Saad-Olivera X., Nesvorný D., Kipping D. M., Roig F., 2017, AJ, 153, 198
Saar S. H., Donahue R. A., 1997, ApJ, 485, 319
Sanchis-Ojeda R., Winn J. N., 2011, ApJ, 743, 61
Sanchis-Ojeda R., Winn J. N., Holman M. J., Carter J. A., Osip D. J., Fuentes C. I., 2011, ApJ, 733, 127
Sanchis-Ojeda R. et al., 2012, Nature, 487, 449
Schlegel D. J., Finkbeiner D. P., Davis M., 1998, ApJ, 500, 525
Seager S., Kuchner M., Hier-Majumder C. A., Militzer B., 2007, ApJ, 669, 1279
Smith A. M. S. et al., 2017, MNRAS, 464, 2708
Sneden C., Bean J., Ivans I., Lucatello S., Sobeck J., 2012, Astrophysics Source Code Library, record ascl:1202.009

Stetson P. B., Pancino E., 2008, PASP, 120, 1332
Telting J. H. et al., 2014, Astron. Nachr., 335, 41
Tull R. G., MacQueen P. J., Sneden C., Lambert D. L., 1995, PASP, 107, 251
Valenti J. A., Fischer D. A., 2005, ApJS, 159, 141
Valenti J. A., Piskunov N., 1996, A&AS, 118, 595
Vanderburg A., Johnson J. A., 2014, PASP, 126, 948
Winn J. N., 2010, Exoplanet Transits and Occultations. University of Arizona Press, Tucson, AZ, p. 55
Zechmeister M., Kürster M., 2009, A&A, 496, 577

This paper has been typeset from a TEX/LATEX file prepared by the author.